nature astronomy

Article

https://doi.org/10.1038/s41550-026-02905-7

Detection of a four-carbon sugar in interstellar space

Received: 11 September 2025

Accepted: 27 May 2026

Published online: 13 July 2026

Check for updates

Izaskun Jiménez-Serra[1] ✉, Juan García de la Concepción[2], Herma M. Cuppen[3], Marta Rey-Montejo[1,4], Miguel Sanz-Novo[1,5], Víctor M. Rivilla[1], Jesús Martín-Pintado[1], Andrés Megías[1], Carlos Briones[1], David San Andrés[1,4], Laura Colzi[1], Shaoshan Zeng[6], Sergio Martín[7,8], Joseph Salaris[3], Antonio Martínez-Henares[1,6], Álvaro López-Gallifa[1], Miguel Angel Requena-Torres[9], Belén Tercero[10,11], Pablo de Vicente[11], Aran Insausti[12,13], Elena R. Alonso[14] & Emilio J. Cocinero[12,13]

Sugars are essential biomolecules, serving as metabolic fuels, nucleic acid backbone components and structural or energy-storage polymers. A central question in origin-of-life research is how monosaccharides formed on the primitive Earth, as laboratory experiments under prebiotic conditions yield insufficient concentrations. The detection of ribose, glucose and other monosaccharides in asteroids and meteorites suggests an exogenous origin, possibly in the interstellar medium (ISM) before meteoritic parent-body formation. However, no sugar has been observed in the ISM so far. Here we report the discovery of erythrulose, a chiral four-carbon ketose, in the ISM. The detection was achieved through ultrasensitive, broadband spectral surveys of the Galactic Centre molecular cloud G+0.693−0.027, using the Yebes 40 m and IRAM 30 m telescopes. Erythrulose appears to be at least eight times more abundant than analogous three-carbon sugars, which remain undetected in our ultrasensitive observations. Quantum chemical and astrochemical models indicate that erythrulose forms efficiently on interstellar dust grains from simpler two-carbon aldehydes and alcohols. As ketoses readily isomerize into aldoses in aqueous conditions, interstellar erythrulose could have contributed to the sugar inventory available for early metabolic and replication processes.

The interstellar medium (ISM) is an impressive chemical factory in which more than 340 molecules have been detected so far[1], including large aromatic species[2–4]. Several of these molecules, such as urea, hydroxylamine and ethanolamine[5–9], are directly connected to origin-of-life chemistry because they are considered precursors of ribonucleosides and lipids[10–13]. Sugars are also central molecules to prebiotic chemistry[11,14,15]; however, they are usually introduced ad hoc (that is, as inputs) in prebiotic reaction schemes because their formation under plausible early-Earth conditions remains inefficient[16–19].

The detection of bio-essential sugars such as ribose and glucose in primitive meteorites and in asteroid Bennu suggests that at least part of the sugar inventory available on the early Earth may have had an exogenous origin[20,21]. A natural possibility is that these sugars, or their precursors, formed before parent-body accretion. However, no sugar has so far been reported in the ISM. Glycolaldehyde ($HOCH_2CHO$) is widespread in interstellar space[22–24] and has often been discussed in this context because of its structural relationship to aldose sugars. Yet, it is a hydroxyaldehyde rather than a true saccharide[25].

A full list of affiliations appears at the end of the paper. ✉e-mail: ijimenez@cab.inta-csic.es

A major obstacle to searching for interstellar sugars has been the lack of accurate gas-phase rotational data. Such data are essential for astronomical identification, but obtaining them was long considered extremely challenging because sugars are thermally fragile and strongly hygroscopic, which hampers their manipulation and conventional thermal vaporization. This limitation has recently been overcome using ultrafast laser vaporization, which enabled the gas-phase rotational characterization of ribose, 2-deoxyribose and erythrulose[26–28]. These laboratory data opened the way to sensitive astronomical searches for sugars with three and four carbon atoms (that is, C3 and C4 sugars)—for example, glyceraldehyde ($HOCH_2CH(OH)CHO$), dihydroxyacetone ($HOCH_2COCH_2OH$) and erythrulose ($HOCH_2CH(OH)COCH_2OH$)—although previous searches remained unsuccessful[6,28–31].

Here, we report the discovery of erythrulose—the only C4 ketose—in the ISM, towards the molecular cloud G+0.693−0.027 (hereafter G+0.693), located in the Galactic Centre region at a distance of ~8.2 kpc from us[32]. The identification was enabled by an ultrasensitive broadband spectral survey with the Yebes 40 m and the IRAM 30 m radiotelescopes covering more than 91 GHz across the 7 mm, 3 mm and 2 mm atmospheric windows (Methods). G+0.693 is one of the richest molecular reservoirs known in the Galaxy[6,33,34] and has yielded numerous detections of new interstellar species of prebiotic interest in recent years[8,35,36].

Results

Detection of erythrulose in G+0.693

Although line blending remains a challenge in chemically rich sources such as G+0.693, the analysis presented here identifies a set of transitions that are consistent with the predicted spectrum of erythrulose. Figure 1 shows 12 sets of lines of erythrulose (accounting for a total of 17 individual transitions) identified in the G+0.693 cloud using the MADCUBA-SLIM software (https://cab.inta-csic.es/madcuba/; see also Extended Data Table 1). These correspond to the brightest and most unblended transitions of erythrulose present in our dataset with integrated intensities ≥9σ—with σ = r.m.s. × $\sqrt{\delta v \times \mathrm{FWHM}}$, where r.m.s. is the root mean square noise level of the spectra, δv is the velocity resolution and FWHM the full width at half maximum of the lines—which are used to fit the erythrulose emission under the assumption of local thermodynamic equilibrium (LTE) using MADCUBA-SLIM (Methods). The individual contribution of the erythrulose transitions is shown in red, while in blue we report the total spectrum predicted by MADCUBA-SLIM considering the contribution from all molecular species identified and modelled towards G+0.693 (more than 180 species, including isotopologues, are considered in the model). Note that transitions from higher vibrational states are not expected in this cloud because the molecular emission is subthermally excited with measured $T_{ex} \leq 15$ K (refs. 34,37).

Six sets of transitions out of the 12 shown in Fig. 1 are classified as predominantly unblended (at 42,023, 40,932, 35,442, 39,782, 40,329 and 33,385 MHz), with contamination levels ≤25% (Extended Data Table 1; the criteria to establish the predominantly unblended features of erythrulose are described in the Methods and Supplementary Information). This ensures that the emission in these features is dominated by erythrulose and provides a robust basis for identification. The transitions at 34,639, 39,073 and 37,060 MHz are classified as blended with U-lines according to our selection criteria (Methods; Extended Data Table 1). However, a visual inspection shows that the erythrulose fit predicted by MADCUBA-SLIM reproduces well the observed spectra (Fig. 1). The features at 44,611, 38,346 and 32,227 MHz are blended with known molecular species, but the agreement with the global fit is excellent, further reinforcing the detection of erythrulose.

Extended Data Fig. 1 shows the remaining transitions of erythrulose present in our dataset with peak intensities ≥1.2 mK, that is, 3× the average r.m.s. noise level in the spectra shown in Fig. 1. These transitions are weaker or more affected by blending and/or noise and are hence not used for the LTE fit of erythrulose. Despite not being used for the LTE fit, all these erythrulose lines predicted by MADCUBA-SLIM are consistent with the observed spectra. Given the physical properties of erythrulose in G+0.693 (see below), its brightest lines are expected to fall within the frequency range covered by Yebes 40 m (31–50 GHz), as observed for other complex organic molecules (COMs)[38]. However, some transitions also appear at 3 mm (Extended Data Fig. 1, blue asterisks), although they are largely blended. The agreement across the full set of detected transitions provides strong, independent validation of the identification.

The fit of the 12 sets of erythrulose transitions shown in Fig. 1 using the MADCUBA-SLIM tool yields an excitation temperature of $T_{ex} = 11.3 \pm 1.8$ K and a column density of $N = (8.7 \pm 0.8) \times 10^{13}$ cm^{-2} for a fixed central radial velocity $v_{LSR} = 69$ km s^{-1} and a linewidth FWHM of 22 km s^{-1} (Methods). The derived column density of $(8.7 \pm 0.8) \times 10^{13}$ cm^{-2} translates into an erythrulose abundance of $(6.4 \pm 0.6) \times 10^{-10}$ assuming an H_2 column density of 1.35×10^{23} cm^{-2} for G+0.693 (ref. 39). Glycolaldehyde (with 2 C atoms) is observed with an abundance in G+0.693 similar to that of erythrulose (Table 1). By contrast, the only C3 sugars, glyceraldehyde and dihydroxyacetone, are not detected in this cloud, with upper limits to their abundance $\leq 4 \times 10^{-11}$ and $\leq 7 \times 10^{-11}$, respectively. Erythrulose appears to be ≥8–17 times more abundant than C3 sugars (Table 1). This is striking, as other chemical families (for example, alcohols, thiols, aldehydes and isocyanates) show an abundance decrease of roughly one order of magnitude with each added carbon atom[35,40–42]. One might consider the triol compound glycerol ($HOCH_2CH(OH)CH_2OH$) as a potential precursor of erythrulose, but this molecule was not detected in our survey either (Table 1).

We can estimate the confidence level of the erythrulose detection in G+0.693 following refs. 43,44. Assuming the confusion limit and Gaussian line profiles, the chance of finding a feature at the v_{LSR} of G+0.693 with a tolerance of ±4 km s^{-1} (that is, the largest velocity shift observed for the molecular line emission in G+0.693)[35,45] is $p = 36\%$ for a velocity coverage equivalent to the FWHM of the erythrulose lines. The detection of each successive line has a probability p^n, where n is the number of unblended transitions. The probability of chance alignment for the six most unblended transitions is then $p^6 = 0.2\%$, providing strong statistical support for the identification of erythrulose. It is important to stress that, although G+0.693 presents line-rich and complex spectra, the molecular emission in this cloud is subthermally excited with low T_{ex}, which yields much lower levels of line blending and line confusion as compared to hotter sources such as massive hot cores and low-mass hot corinos. Even if three or four unblended lines were considered in our analysis, we would still obtain confidence levels of 95.2% and 98.3%, respectively. Note that this estimate is conservative because line confusion has not been reached in our G+0.693 spectral surveys.

Formation mechanism on interstellar ice surfaces

The C3 sugars glyceraldehyde and dihydroxyacetone are at least 8–17 times less abundant than erythrulose, suggesting that they are unlikely to be its dominant precursors under the physical conditions of G+0.693. Therefore, we turn our attention to smaller and more abundant building blocks of this C4 sugar such as glycolaldehyde and ethylene glycol. Recent laboratory experiments of irradiated CH_3OH ices reveal that sugars with up to six carbon atoms can be produced from smaller sugar and sugar-derivative fragments (that is, C6 sugars would form from C3 sugar precursors)[46]. By inspecting the chemical structure of erythrulose, one can envision its formation via the combination of two C2 fragments: $CH_2OHC^{\bullet}O$ and $C^{\bullet}HOHCH_2OH$. The first fragment is the glycolaldehyde radical (g*), and the second is the ethylene glycol radical (e*), which contains a pro-chiral centre at carbon C$^{\bullet}$, responsible for the chirality of erythrulose. Both glycolaldehyde and ethylene glycol are present in G+0.693 at high abundances; their measured abundances are $(6.9 \pm 0.2) \times 10^{-10}$ and $(1.7 \pm 0.4) \times 10^{-9}$, 1.1 and 2.7 times the erythrulose abundance, respectively (Table 1). Moreover, the radical g* has

https://doi.org/10.1038/s41550-026-02905-7

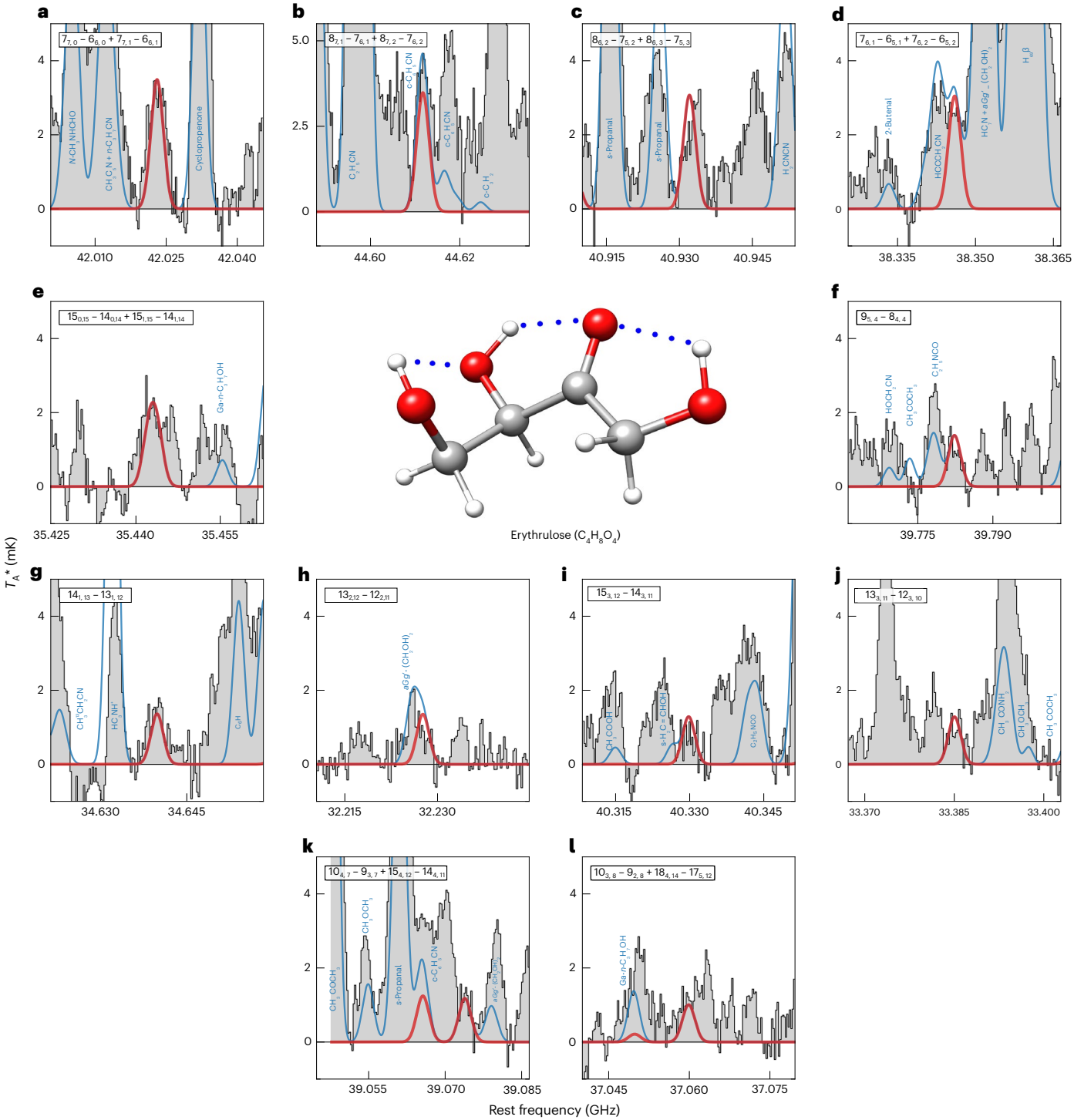


Fig. 1 | Brightest and most unblended transitions of erythrulose observed towards the G+0.693 molecular cloud. a–l, Filled histograms report the observed spectra, red lines show the line profiles of the erythrulose transitions fitted with MADCUBA-SLIM, and blue lines present the total fit to the spectra considering all the molecules identified towards the cloud. The intensity of the observed spectra is shown in units of antenna temperature, T_A^*. The quantum numbers of each transition of erythrulose are given in the upper part of each graph. Blue labels indicate the molecular species contributing to the observed spectra in the vicinity of the erythrulose lines. The transitions are sorted from the brightest to the weakest lines according to the LTE model.

been identified as the main intermediate species formed in laboratory experiments simulating the reaction of atomic H with glycolaldehyde in solid para-H_2 (dense cloud conditions)[47]. Besides, sugar acids have also been synthesized experimentally by the energetic processing of interstellar ice analogues containing ethylene glycol and CO_2, through the formation of the radical e* (ref. 48). Therefore, the combination of g* and e* could lead to the synthesis of erythrulose in the ISM.

Figure 2 illustrates the formation mechanism of this C4 ketose sugar on the surface of amorphous solid water ice (ASW) from the radicals g* and e*. This formation mechanism has two isoenergetic mirror symmetry mechanisms that form the two enantiomers with 50% probability each. Figure 2a shows the most favourable orientation of the glycolaldehyde–ethylene glycol complex (g–e) on the ASW and all possible reactive collisions of atomic H with the complex. Among these,

Table 1 | Derived physical parameters and modelled abundances of erythrulose and chemically related species towards the G+0.693 molecular cloud

Molecule	N	T_{ex}	v_{LSR}	FWHM	χ^{a}_{obs}	χ^{d}_{mod}
	($\times10^{13}$ cm^{-2})	(K)	(km s^{-1})	(km s^{-1})	($\times10^{-10}$)	($\times10^{-10}$)
Glycolaldehyde ($HOCH_2CHO$)[b]	9.3 ± 0.3	21.8 ± 0.8	68.9 ± 0.2	19.4 ± 0.5	6.9 ± 0.2	~20
aGg′-ethylene glycol [aGg′-$(CH_2OH)_2$]	23.5 ± 5.2	10.3 ± 2.6	67.9 ± 2.8	21[c]	17.4 ± 3.9	~100
Glyceraldehyde ($HOCH_2CH(OH)CHO$)	≤0.5	10[c]	69[c]	21[c]	≤0.4	~20
Dihydroxyacetone ($HOCH_2COCH_2OH$)	≤1.0	10[c]	69[c]	21[c]	≤0.7	~50
Glycerol ($HOCH_2CH(OH)CH_2OH$)	≤2.5	10[c]	69[c]	21[c]	≤1.9	~1
Erythrulose ($HOCH_2CH(OH)COCH_2OH$)	8.7 ± 0.8	11.3 ± 1.8	69[c]	22[c]	6.4 ± 0.6	~20

[a]Molecular abundances calculated using $N(H_2)=1.35\times10^{23}$ cm^{-2} (ref. 39). [b]Derived physical parameters taken from ref. 9. [c]This parameter was fixed in MADCUBA SLIM-AUTOFIT to reach convergence. [d]Modelled abundances at 1.6 Myr from the simulation with $\zeta=1.3\times10^{-14}$ s^{-1}.

the hydrogen abstraction reaction 3-g−e, is the fastest reaction (Fig. 2a, green), with an energy barrier of 4.1 kJ mol^{-1} and a reaction energy of 27.4 kJ mol^{-1} (zero-point energy corrected; see the Supplementary Information for further details). The quantum tunnelling-corrected rate constant of reaction 3-g−e ranges from 3.1×10^{10} s^{-1} to 1.2×10^{12} s^{-1} in the temperature range of 20–300 K (Fig. 2e), and hence it is a very fast reaction.

After the H abstraction reaction 3-g−e, the activated glycolaldehyde complex (g*−e; Fig. 2b) is formed, which could proceed with either subsequent H abstraction reactions or two isomerization reactions by hydrogen migration to the activated carbon of the aldehyde group. The two isomerization reactions present energy barriers of 77.0 and 97.3 kJ mol^{-1}, which makes them non-viable under ISM conditions. For the H abstraction reactions, reaction 1-g*−e shows a repulsive potential (Supplementary Information). However, reactions 2-g*−e and 3-g*−e are energetically favoured and form hydroxyketene for reaction 2-g*−e, and the doubly activated complex g*−e* for reaction 3-g*−e (Fig. 2c). The branching ratios for these two reactions are approximately 50% in the whole range of temperatures, being slightly higher for the formation of the g*−e* complex at low temperatures (Fig. 2g). The tunnelling-corrected rate constant of reaction 3-g*−e ranges from 9.7×10^{6} s^{-1} to 2.5×10^{9} s^{-1} between 20 K and 300 K.

Once formed, the g*−e* complex is in the triplet state and the radicals cannot recombine because the approach of atoms having parallel electrons induces a repulsive potential. However, the g*−e* complex can experience a spin change under ISM conditions throughout an intersystem crossing (ISC) process, because both states are practically degenerate with an energy difference (zero-point energy corrected) of only 0.04 kJ mol^{-1} in favour of the singlet state (Supplementary Information). The latter process shows rate constants of 2.4×10^{5} s^{-1}–1.6×10^{7} s^{-1} between 20 K and 300 K, making it the slowest step in the entire reaction mechanism (Fig. 2h and Supplementary Table 2). Finally, the association of the two carbons with antiparallel spin yields erythrulose (Fig. 2d).

Astrochemical modelling of erythrulose formation

We have demonstrated that erythrulose can form on the surface of interstellar dust grains from glycolaldehyde and ethylene glycol at a rate constant of $(1–2)\times10^{5}$ s^{-1} at the typical dust temperatures measured in Galactic Centre molecular clouds ($T_{dust}\approx20–30$ K)[49,50]. Using this information, we now evaluate whether we can predict the observed amount of erythrulose in the G+0.693 cloud by implementing the mechanism described above in a kinetic Monte-Carlo (KMC) simulation code[51–54]. We expanded our chemical network to include the formation of other C3 and C4 sugars (glyceraldehyde, dihydroxyacetone, threose and erythrose) and related compounds (for example, glycerol). The network allows radicals from C1 and C2 species (for example, H$^{\bullet}$CO, $H_2C^{\bullet}OH$, HC$^{\bullet}$OHCHO, CHOHC$^{\bullet}$O and $CH_2OHC^{\bullet}HOH$) to recombine[54], forming five different C3 compounds (including the sugars dihydroxyacetone and glyceraldehyde, plus glycerol and two C3 aldehydes) and six different C4 compounds (including threose and erythrulose). Additional hydrogen abstraction, hydrogenation and ultraviolet (UV) photodissociation reactions (including those inducing the breaking of the CC bond of glycolaldehyde and ethylene glycol) were added to allow the interconversion between species (Methods). We ran simulations of the ice build-up for different cosmic-ray ionization rates: $\zeta=1.3\times10^{-17}$ s^{-1} (the standard Galactic value) and 1.3×10^{-15} s^{-1} and 1.3×10^{-14} s^{-1} (100 and 1,000 times higher, as applicable to Galactic Centre molecular clouds[55,56]). The model assumes an initial hydrogen-nuclei density of 10^{3} cm^{-3}, rising to 2×10^{4} cm^{-3} over 1.5 Myr during the collapse of the cloud, after which the density is kept constant (Fig. 3). We fix the dust temperature at $T_{dust}=20$ K, consistent with observations of G+0.693 (ref. 50). Each simulation was run with nine different random seeds.

Figure 3 shows that both C3 and C4 sugars can form efficiently in the ice in our models. Erythrulose is the most efficiently produced C4 sugar, achieving higher abundance than the C4 aldoses (threose and erythrose) under most conditions. Consistent with our observations, erythrulose tends to reach slightly higher abundances than the C3 sugars (glyceraldehyde and dihydroxyacetone), especially at higher ζ and shorter timescales. This behaviour results from the higher UV photodestruction rate assumed for C3 sugars compared with C4 sugars (Methods). Chemically, smaller sugar molecules are expected to be more easily destroyed than larger ones, as larger molecules have more degrees of freedom to distribute energy upon UV absorption. In our simulations, ethylene glycol is always more abundant than any C3 and C4 sugar, in agreement with our observations. Glycolaldehyde, however, reaches abundances comparable to, or slightly higher than, those of the C3 and C4 sugars only towards the end of the simulations.

Molecular clouds in the Galactic Centre are pervaded by low-velocity shocks from cloud shearing and collisions[57]. G+0.693 is believed to be undergoing such a collision, driving a large-scale shock of $v_s\approx20$ km s^{-1} (ref. 37). Ice material is thus expected to be partially injected into the gas phase in G+0.693 by grain sputtering[58]. Figure 3 shows that the KMC models whose ice abundances come closest to the observed gas-phase values in G+0.693 are those with $\zeta\geq1.3\times10^{-14}$ s^{-1}. Such high values of ζ were also invoked in previous models of this source to explain the abundances of certain molecular ions (for example, PO^{+} and $HOCS^{+}$)[59,60]. In our simulations, the predicted abundances in the ice of CH_3OH, glycolaldehyde, ethylene glycol and erythrulose all lie within a factor of 5 of the observed values (Table 1) and well within the tolerance of one order of magnitude typically considered in chemical modelling. The C3 sugars (glyceraldehyde and dihydroxyacetone) are overproduced in the model by factors of ~25–70. However, the abundance ratios of glycolaldehyde, ethylene glycol, and the C3 sugars with respect to erythrulose differ by slightly more than one order of magnitude (Table 2), while remaining broadly consistent given the large uncertainties in our simulations.

https://doi.org/10.1038/s41550-026-02905-7

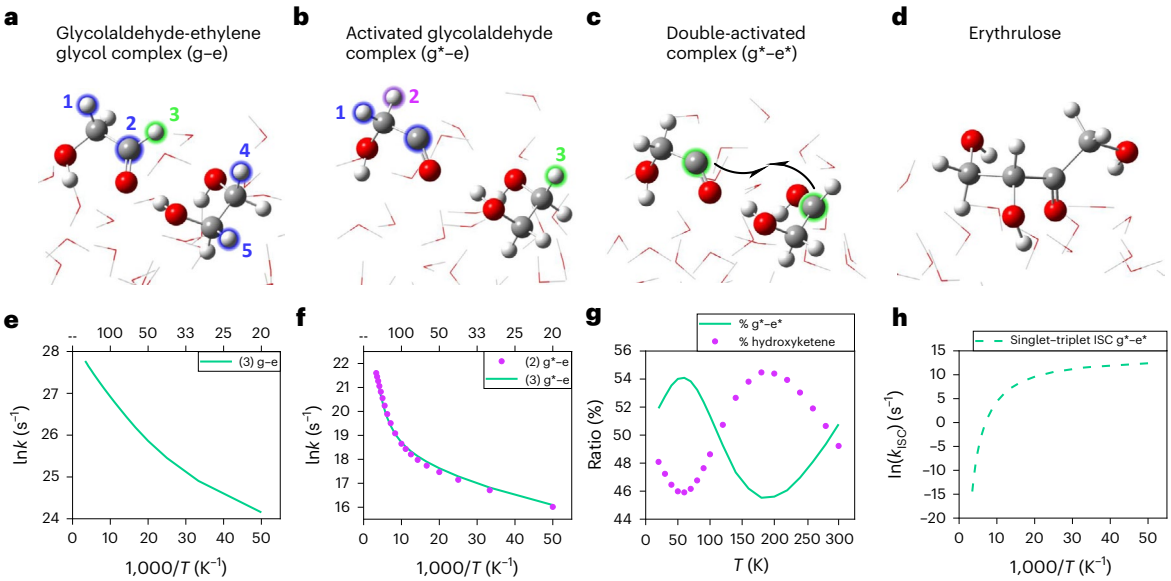


Fig. 2 | Reaction mechanism of erythrulose from glycolaldehyde (g) and ethylene glycol (e) on ASW. a–**d**, Optimized geometries are shown for the complexes g–e (**a**), the first activated g*–e complex (**b**), the doubly activated g*–e* complex (**c**) and erythrulose (**d**). The available hydrogen and carbon atoms for abstraction, addition and recombination reactions are highlighted in blue, green and purple. The green and purple highlighted hydrogen atoms in **a** and **b** represent, respectively, the most viable reactions. Green carbon atoms in **c** represent the recombination of the two radicals. **e**,**f**, Arrhenius plots of the thermal rate constants for reaction 3-g–e (**e**) and reactions 2-g*–e and 3-g*–e (**f**). **g**, The branching ratios for reactions 2-g*–e and 3-g*–e leading to the complexes hydroxyketene–ethylene glycol (not shown) and g*–e*. **h**, The rate constant for the ISC of the g*–e* complex. Some water molecules have been removed from the images of the optimized geometries for the sake of clarity.

The discrepancy between the modelled abundances in the ice and the observed abundances in the gas could be due to a combination of effects. First, only a fraction of the ices may be sputtered in the shock (≤30%, based on the KMC results). C3 and C4 sugars are more refractory than water and, hence, may be harder to eject from grains. Alternatively, C3 and C4 sugars may rapidly re-adsorb onto dust grains given the low dust temperature (T_{dust} = 20 K) in G+0.693. This could result in less of those sugars remaining in the gas to be observed. The detection of CO and CO_2 ice in Galactic Centre molecular clouds[61] indicates that a fraction of the ices remain on dust grains despite the dust energetic processing. In addition, note that the KMC simulations do not include an extended gas-phase chemical network for these COMs and, hence, C3 and C4 sugars may undergo efficient gas-phase destruction through ion-neutral reactions[60] after the ice release in the shock. Glyceraldehyde has recently been found to be more unstable than glycolaldehyde in the gas phase, which may explain its lack of detection[62]. Finally, uncertainties in reaction rates (for example, photodissociation efficiencies)[63], reaction branching ratios or even unmodelled processes might also play a role in overestimating sugar abundances in the ice in our model.

Discussion

Erythrulose, with 14 atoms in its structure, represents the largest non-cyclic molecular species identified so far in the ISM (cf. ref. 64), and the first detected molecule containing four oxygen atoms (cf. the catalogue in ref. 1). It is also the first sugar and the second chiral molecule reported in the ISM after that reported in ref. 65. Its detection not only provides direct evidence that complex, chiral species can form under interstellar conditions, but it also takes us to a higher level in the ladder of interstellar chemical complexity, suggesting that other prebiotic (and potentially chiral) molecules could also form and survive under the extreme conditions of the ISM.

Prebiotic chemistry experiments have shown that ribonucleotides—the building blocks of RNA—can be synthesized from mixtures containing sugars such as erythrulose[66]. Ketoses such as erythrulose can readily isomerize into their aldose counterparts (that is, threose and erythrose) in aqueous environments[67], a transformation that is central to the formation of ribose and then nucleic acids[68]. However, prebiotic experiments have typically introduced such sugars as external inputs. Our detection of erythrulose in the G+0.693 molecular cloud demonstrates that this monosaccharide can be synthesized abiotically under interstellar conditions. The similarity of the organic inventories of comets and presolar environments supports a connection between the chemistry observed in the ISM and that inherited by minor bodies of the Solar System[69]. Therefore, the detection of interstellar erythrulose suggests that complex sugars may have formed in the protosolar molecular cloud and were subsequently transferred to minor bodies.

Sugars such as ribose and glucose have indeed been found in meteorites[20] and in asteroid Bennu[21]. In addition, erythrulose has also been proposed to exist on the surface of outer Solar System bodies, including the Kuiper Belt object Arrokoth[46]. Laboratory irradiation experiments support the interstellar formation of erythrulose, as well as other sugar derivatives such as sugar acids and sugar alcohols[46,48], in agreement with our astrochemical model. Our astrochemical simulations indeed show that erythrulose can form efficiently in ices under a range of cosmic-ray ionization rates, including those expected in dust traps of protoplanetary disks[70]. In these regions, energetic processing transforms simple ices into macromolecular organics, with up to 4% of the ice reservoir affected[70]. Hence, once formed, erythrulose and other sugars may be incorporated into planetesimals (as measured in Arrokoth[46] and meteorites[20]), later contributing to the inventory of prebiotic organic material on planetary surfaces. The discovery of chiral erythrulose also supports the idea that small enantiomeric excesses measured in meteorites (of a few per cent)[71,72] may originate in extraterrestrial environments, which could have contributed to the emergence of biological homochirality on early Earth through subsequent chemical amplification processes[73].

Even under conservative assumptions—considering only the observed gas-phase abundance of erythrulose in G+0.693—and given the interstellar water abundance of 10^{-4} (see ref. 74), the erythrulose/water abundance ratio measured in G+0.693 is of ~6×10^{-6}. Other

https://doi.org/10.1038/s41550-026-02905-7

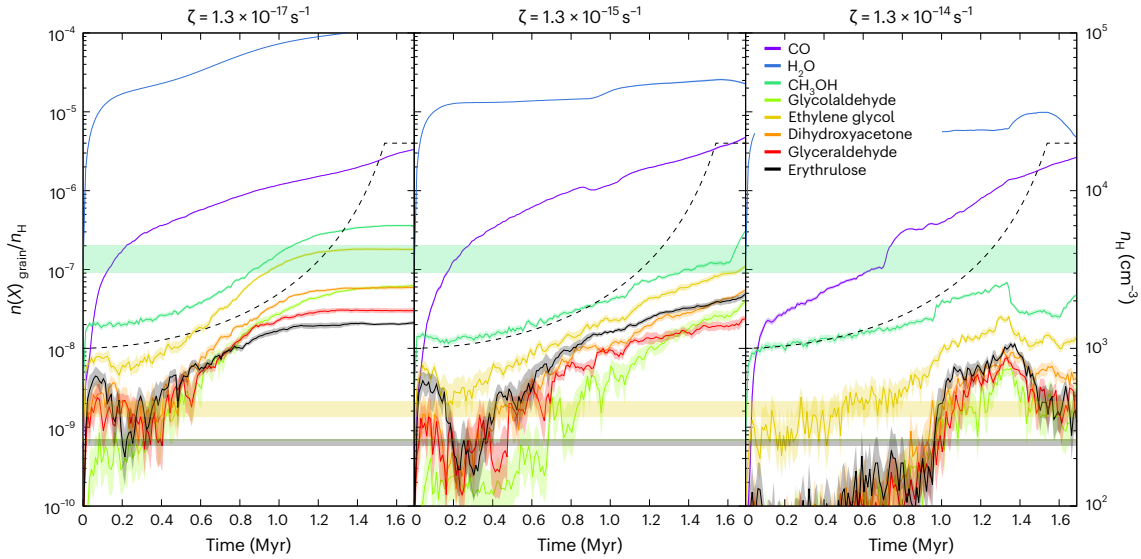


Fig. 3 | KMC simulations of the ice build-up in a cloud with similar physical conditions to those of G+0.693. Colour lines indicate the solid ice abundances of CO, H_2O, CH_3OH, glycolaldehyde, ethylene glycol and all C3 and C4 sugars considered in the model (Methods). The ratio $n(X)_{grain}/n_H$ refers to the molecular fractional abundance measured with respect to hydrogen nuclei, n_H. $n(X)_{grain}$ is the volume density of molecule X in the ice in units of cm^{-3}. Data are presented as mean values ± 1 standard deviation spread of the nine simulations carried out with different random seeds. Labels are shown on the right, and the cosmic-ray ionization rate, ζ, is presented at the top of each panel. Dashed lines indicate the increase of the gas density during the cloud's collapse. Horizontal colour-shaded ranges show the molecular abundance values measured towards G+0.693 together with their 1σ uncertainty (Table 1).

Table 2 | Observed and predicted abundance ratios with respect to erythrulose

Abundance ratio	Observed	Modelled	Observed / Modelled
Glycolaldehyde/erythrulose	1.1	~1	~1
Ethylene glycol/erythrulose	2.7	~5	~0.5
Erythrulose/glyceraldehyde	≥17.4	~1	≥17
Erythrulose/dihydroxyacetone	≥8.7	~0.4	≥22

The predicted abundances are taken from the model with $\zeta \geq 1.3 \times 10^{-14}\,s^{-1}$ at ~1.6 Myr.

prebiotic organics such as ethanolamine, also detected in G+0.693, have been found in meteorites with abundance ratios with respect to water similar to those measured in the ISM[8]. Therefore, considering that the average water content in meteorites is 7,500 ppm (ref. 75) and an estimated amount of organic matter delivered to early Earth of 10^{16}–10^{18} kg (ref. 76), we estimate that ~(0.5–50) × 10^9 kg of erythrulose could have been delivered to early Earth during the Late Heavy Bombardment between 4.1 and 3.9 billion years ago[77]. Although the extent and intensity of the Late Heavy Bombardment has recently been questioned[78], Monte-Carlo simulations of Earth's impact history show that biopoiesis—the process describing the development of living matter from non-living organic matter—could occur within a much broader timeline between 4.45 and 3.9 billion years ago with at least a 16% chance[79]. Because glycolaldehyde, small sugars and sugar derivatives have been shown to survive meteoritic impacts[80,81], the presence of erythrulose in interstellar space strengthens the case for an exogenous origin of sugars relevant to the synthesis of the first nucleic acids. The presence of erythrulose on the surface of a primitive Earth and its rapid isomerization into threose[67] support its involvement in the formation of threose nucleic acid (TNA), a structurally simpler RNA analogue and the simplest of all potential sugar-containing nucleic acids. Threose nucleic acid has been synthesized in the laboratory and, in the context of the origin of life, has been proposed as one of the polymers that could have been involved in a pre-RNA world[82]. Therefore, the discovery of interstellar erythrulose suggests that the ISM could be a viable source of sugar feedstock for the prebiotic synthesis of the first nucleic acids, not only on the primitive Earth but also elsewhere in the Universe.

Methods

Observational campaign and spectral coverage

We conducted a broadband, ultrasensitive spectral survey of the Galactic Centre molecular cloud G+0.693 using the Yebes 40 m (Guadalajara, Spain) and IRAM 30 m (Granada, Spain) radiotelescopes. Observations were performed in position-switching mode towards α(J2000) = 17 h 47 min 2 s, δ(J2000) = −28° 21′ 27″, with α the right ascension and δ the declination of the source, and using an off position shifted by $\Delta\alpha$ = −885″ and $\Delta\delta$ = 290″. The Yebes 40 m data (project 21A014) were collected between March 2021 to March 2022 using the ultrabroadband Nanocosmos Q band (7 mm) HEMT receiver, which provides full frequency coverage from 31.07 to 50.42 GHz in two linear polarizations[83]. Spectra were recorded using the 16 fast Fourier transform spectrometers (38 kHz channel width), with frequency set-ups at 41.4 and 42.3 GHz to flag spurious features. Data reduction and averaging were performed using the Python-based pipeline (https://github.com/andresmegias/gildas-class-pipeline/) developed by ref. 84 and the MADCUBA software (https://cab.inta-csic.es/madcuba/index.html; see ref. 85). The final spectra were smoothed to a frequency resolution of 256 kHz (1.5–2.5 km s^{-1}). The half power beam width of the telescope ranged between 35″ and 55″. All data were calibrated in T_A^* units because the molecular emission towards G+0.693 is extended over the beam[33,34]. The final r.m.s. noise achieved was 0.25–0.9 mK per channel.

The IRAM 30 m observations (projects 123-22 and 076-23) were performed during different sessions in 2023 (February) and 2024 (March and April) using the Eight Mixer Receivers (EMIR). Spectral coverage spanned 83.2–115.41, 132.28–140.39 and 142–173.81 GHz. Each frequency set-up was shifted in frequency to identify possible contamination of spurious lines coming from the image band. The fast Fourier transform spectrometer (FTS200) provided a spectral resolution of 195 kHz, although the spectra were subsequently smoothed to 615 kHz (1.0–2.2 km s^{-1}). The spectra were calibrated in T_A^* units. The half power beam width ranged from 14″ to 29″. The final r.m.s. noise was 0.5–2.5 mK at 3 mm and 1.0–1.6 mK at 2 mm per channel. Frequency gaps were filled using data from previous IRAM surveys[36,40].

Identification of predominantly unblended transitions

The rotational spectrum of the L-1 conformer of erythrulose—the lowest-energy open-chain conformer—was measured in the laboratory by ref. 28. Its spectroscopic entry was calculated using SPCAT up to 720 GHz. Predicted frequencies below 18 GHz have uncertainties as low as 1 kHz, which translates into errors of up to 120 kHz in the Q band, equivalent to ~0.7–1.2 km s^{-1}. These uncertainties are much smaller than the typical linewidths (of ~20 km s^{-1}) observed in G+0.693 and than the spectral resolution of our data (minimum of 256 kHz). A similar approach has been used for the discovery of several other molecular species in this cloud, even when using spectra at higher frequencies (for example, at 3 mm; see the case of $HOCS^+$)[60,86].

The SPCAT spectroscopy entry was incorporated into the MADCUBA package (version 31/05/2024)[85], and transitions of erythrulose were identified using the Spectral Line Identification and Modeling (SLIM) tool under the assumption of LTE. SLIM generates the LTE synthetic spectra for comparison with observed data. This allows us to identify the brightest and most unblended transitions of erythrulose shown in Fig. 1. The line classification has been carried out following the criteria described in ref. 87, which are based on the accepted standard of ref. 43 and ref. 44:

(1) Accurate rest frequencies: The frequency uncertainties of the identified erythrulose transitions are ≤120 kHz (see values in parentheses within the first column of Extended Data Table 1), which lies below the spectral resolution of our Yebes 40 m and IRAM 30 m data with a minimum value of 256 kHz.
(2) Frequency agreement: "An accurate astronomical rest frequency of the assigned transition must be in reasonable agreement with the frequency corresponding to the LSR velocity of the source"[43]. The erythrulose emission is well reproduced by fixing its V_{LSR} to 69 km s^{-1} (Table 1), in excellent agreement with the V_{LSR} obtained for other COMs towards G+0.693 (ref. 34).
(3) Linewidth agreement: The derived linewidth of the erythrulose lines is 22 km s^{-1} (Table 1). This value is consistent with those observed for other molecules towards the G+0.693 cloud[88].
(4) Beam dilution: Our data do not suffer from beam dilution because the emission of COMs such as glycolaldehyde and ethylene glycol towards G+0.693 is extended across the Sgr B2 molecular cloud[89] and, therefore, across the single-dish beams of the IRAM 30 m and Yebes 40 m telescopes.
(5) Relative intensities: "Once several molecular transition assignments have been made, their relative intensities must be tested for consistency"[43]. All observed spectral features are consistent with the LTE predictions obtained with MADCUBA-SLIM (Fig. 1 and Extended Data Fig. 1).
(6) Confirmation of transitions: "There must be spectral features at all favorable, physically connected transitions over a sufficiently large wavelength range". Our dataset covers over 91 GHz in the 7 mm, 3 mm and 2 mm wavelength ranges, and all predicted features of erythrulose are consistent with the observed spectra. Note that the global LTE fit overpredicts the spectrum for the $17_{0,17} \rightarrow 16_{0,16}$ and $17_{1,17} \rightarrow 16_{1,16}$ transitions at ~40.070 GHz (Extended Data Fig. 1y), but this can be considered an outlier in our model. Other blended transitions such as the $12_{5,7} \rightarrow 11_{4,7}$ and $15_{4,11} \rightarrow 14_{4,10}$ transitions (Extended Data Fig. 1m,ff), and the $14_{11,3} \rightarrow 13_{10,3}$+$14_{11,4} \rightarrow 13_{10,4}$ and $10_{3,7} \rightarrow 9_{2,7}$+$9_{3,7} \rightarrow 8_{2,7}$ line sets (Extended Data Fig. 1s,bb), match the observed spectra very well.
(7) Level of blending: To determine the level of blending with other molecules or U-lines, we obtained the residual area after subtracting the LTE fit of the erythrulose lines from the total measured area in the observed spectra, over the velocity range defined by V_{LSR} = 69 ± FWHM (that is, over 2 × FWHM). This velocity range covers 98.2% of the total area underneath a Gaussian line profile. As shown in Supplementary Fig. 2, if one considers the most unfavourable case in which the observed spectral feature is flat due to heavy line blending, the derived residual area would represent ~50% the total area measured over a velocity range of 2 × FWHM. Therefore, we establish a criterion whereby an observed feature is considered mostly unblended if the residual contribution is less than half this limit, that is, ≤25% (Supplementary Information). A similar approach has been adopted in recent detections of new molecules in G+0.693, including large complex organics[38,87].

Following these criteria, we identify a total of six mostly unblended features, which account for nine individual transitions of erythrulose. Although blended with residual emission ≥25%, the visual inspection of Fig. 1b,d,h shows that the global LTE fit reproduces well the observed spectra for the sets of transitions $8_{7,1} \rightarrow 7_{6,1}$+$8_{7,2} \rightarrow 7_{6,2}$, and $7_{6,1} \rightarrow 6_{5,1}$+$7_{6,2} \rightarrow 6_{5,2}$, and for the $13_{2,12} \rightarrow 12_{2,11}$ line. All these transitions, together with the consistency of the remaining lines shown in Fig. 1 and in Extended Data Fig. 1, yield a robust assignment of erythrulose. Full line parameters of the transitions shown in Fig. 1 are listed in Extended Data Table 1.

LTE analysis with MADCUBA

We performed a nonlinear least-squares LTE fit of the erythrulose emission by applying the AUTOFIT tool based on the Levenberg–Marquardt algorithm within SLIM[85] to derive the best-fit physical parameters: excitation temperature (T_{ex}), radial velocity (υ_{LSR}), linewidth (FWHM) and column density (N). To achieve convergence, the FWHM of the erythrulose emission had to be fixed to 22 km s^{-1}, consistent with the typical line profiles in G+0.693 (refs. 33,34). Derived values are reported in Table 1 and agree with those obtained for other COMs in this source[33,34].

Computational methods

We simulated the ASW ice by carrying out molecular dynamic simulations of 100 water molecules at 300 K to amorphize the system, which was then cooled at 10 K to preserve the amorphous structure. Because our mechanistic approach involves the non-diffusive association of activated glycolaldehyde (g) and ethylene glycol (e) on ASW ice (Fig. 2), we placed several glycolaldehyde molecules around ethylene glycol and optimized each pair, obtaining only two stable structures: one with a carbonyl–hydroxyl interaction (CO) and another with a hydroxyl–hydroxyl interaction (OH). The two optimized CO and OH structures were used as fragments in a rigid docking study to generate glycolaldehyde–ethylene glycol complexes placed across the ASW surface (Fig. 2). Binding energies for both types were similar overall, but the CO complex showed a higher maximum interaction energy, so its strongest-bound structure was selected for the mechanistic study (Supplementary Fig. 3). Electronic structure calculations were performed with Gaussian 16[90] using a three-layer ONIOM method (PW6B95(D3)/def2-TZVP:PM7R6:UFF)[91–94] to model the reaction mechanism on ASW ice. Reactivity was initiated via hydrogen abstraction reactions forming radicals on the surface. The ISC needed to form erythrulose was studied using CASSCF(6e,5o)/def2-TZVP in ORCA[95,96]. The unimolecular rate constants for the hydrogen abstraction reactions were studied using transision state theory using the Pilgrim software[97]. Tunnelling corrections were applied using the Eckart approximation[98]. The ISC rate of the g*–e* intermediate was estimated using Marcus' semi-classical theory[99,100]. The details of these calculations can be found in the Supplementary Information.

Grain-surface chemistry simulations using the KMC approach

We extended a previously established grain-surface network[54,101] to include six C3-forming radical-radical reactions (leading to, for example, tartonaldehyde, hydroxypyruvaldehyde, glyceraldehyde, dihydroxyacetone and glycerol) and seven C4-forming reactions (leading to 2,3-dihydroxybutanedial, 2,4-dihydroxy-3-oxobutanal, tetrose,

dimethylolglyxoxal, erythrulose and tetritol). The rate constant is estimated to be 2×10^6 s^{-1}. Additional hydrogenation reactions and abstraction reactions ($k = 10^5$ s^{-1}) were included to allow interconversion via radical intermediates[102]. The C3 radicals can react with HC˙O and C˙H$_2$OH to C4 sugar and sugar-derivative species. The glycolaldehyde–ethylene glycol complex was also included explicitly in the model to account for the surface reactions outlined in Fig. 2 (rate constants from Supplementary Table 2). All photodissociation processes were modelled using canonical rate constants of the following form.

For C2 species:

$$k = 10^{-9} \exp(-2.5A_V) + 500\zeta \text{ s}^{-1}; \quad (1)$$

for C3 species:

$$k = 9.0 \times 10^{-10} \exp(-2.5A_V) + 450\zeta \text{ s}^{-1}; \quad (2)$$

for C4 species:

$$k = 8.1 \times 10^{-10} \exp(-2.5A_V) + 405\zeta \text{ s}^{-1}. \quad (3)$$

The slightly reduced photodissociation rates for C4 species reflect their greater resilience due to higher internal degrees of freedom. The grain-surface chemistry is triggered by deposition of H, H$_2$, C, N, O, CO, N$_2$ and O$_2$. Their fluxes are calculated self-consistently, assuming that these represent the main elemental reservoirs in the gas phase, with the remainder residing on grain surfaces. UCLCHEM (https://uclchem.github.io/v3.5.5/; see ref. 103) is used to determine the time-dependent gas-phase CO/C, O$_2$/O and N$_2$/N ratios and H and H$_2$ fluxes.

Data availability

This Article makes use of data from projects 21A014 (Yebes 40 m), and 123-22 and 076-23 (IRAM 30 m). The observed spectra and LTE fits of the transitions of the different species presented in this work are available via Zenodo at https://doi.org/10.5281/zenodo.20081358 (ref. 104). The spectroscopic information of erythrulose can be found in ref. 28.

Code availability

The MADCUBA software is publicly available at https://cab.inta-csic.es/madcuba/. A description of the package is provided in ref. 85. The Python-based script developed by ref. 84 is available via GitHub at https://github.com/andresmegias/gildas-class-python/. UCLCHEM can be downloaded freely from https://uclchem.github.io/. The KMC code is available on reasonable request to H.M.C.

References

1. McGuire, B. A. 2021 census of interstellar, circumstellar, extragalactic, protoplanetary disk, and exoplanetary molecules. *Astrophys. J. Supp. Series* **259**, 30 (2022).
2. Cernicharo, J. et al. Pure hydrocarbon cycles in TMC-1: discovery of ethynyl cyclopropenylidene, cyclopentadiene, and indene. *Astron. Astrophys.* **649**, L15 (2021).
3. Wenzel, G. et al. Discovery of the seven-ring polycyclic aromatic hydrocarbon cyanocoronene ($C_{24}H_{11}CN$) in GOTHAM observations of TMC-1. *Astrophys. J. Lett.* **984**, L36 (2025).
4. Fuentetaja, R. et al. Discovery of 1*H*-cyclopent[cd]indene (c-C11H8) in TMC-1 with the QUIJOTE line survey: a new three-ringed polycyclic aromatic hydrocarbon. *Astron. Astrophys.* **706**, L10 (2026).
5. Belloche, A. et al. Re-exploring molecular complexity with ALMA (ReMoCA): interstellar detection of urea. *Astron. Astrophys.* **628**, A10 (2019).
6. Jiménez-Serra, I. et al. Toward the RNA-world in the interstellar medium—detection of urea and search of 2-amino-oxazole and simple sugars. *Astrobiology* **20**, 1048–1066 (2020).
7. Rivilla, V. M. et al. Prebiotic precursors of the primordial RNA world in space: detection of NH_2OH. *Astrophys. J. Lett.* **899**, L28 (2020).
8. Rivilla, V. M. et al. Discovery in space of ethanolamine, the simplest phospholipid head group. *Proc. Natl Acad. Sci. USA* **118**, e2101314118 (2021).
9. Rivilla, V. M. et al. Precursors of the RNA world in space: detection of (*Z*)-1,2-ethenediol in the interstellar medium, a key intermediate in sugar formation. *Astrophys. J. Lett.* **929**, L11 (2022).
10. Ruiz-Mirazo, K., Briones, C. & de la Escosura, A. Prebiotic systems chemistry: new perspectives for the origins of life. *Chem. Rev.* **114**, 285–366 (2014).
11. Becker, S. et al. Unified prebiotically plausible synthesis of pyrimidine and purine rna ribonucleotides. *Science* **366**, 76–82 (2019).
12. Menor Salván, C. et al. Prebiotic origin of pre-RNA building blocks in a urea "warm little pond" scenario. *ChemBioChem* **21**, 3504–3510 (2020).
13. Fiore, M. et al. Synthesis of phospholipids under plausible prebiotic conditions and analogies with phospholipid biochemistry for origin of life studies. *Astrobiology* **22**, 598–627 (2022).
14. Powner, M., Gerland, B. & Sutherland, J. Synthesis of activated pyrimidine ribonucleotides in prebiotically plausible conditions. *Nature* **459**, 239–242 (2009).
15. Patel, B. H., Percivalle, C., Ritson, D. J., Duffy, C. D. & Sutherland, J. D. Common origins of RNA, protein and lipid precursors in a cyanosulfidic protometabolism. *Nat. Chem.* **7**, 301–307 (2015).
16. Mizuno, T. & Weiss, A. H. in *Advances in Carbohydrate Chemistry and Biochemistry* (eds Tipson, R. S. & Horton, D.) Vol. 29, 173–227 (Academic Press, 1974).
17. Kopetzki, D. & Antonietti, M. Hydrothermal formose reaction. *New J. Chem.* **35**, 1787–1794 (2011).
18. Delidovich, I. V., Simonov, A. N., Taran, O. P. & Parmon, V. N. Catalytic formation of monosaccharides: from the formose reaction towards selective synthesis. *ChemSusChem* **7**, 1833–1846 (2014).
19. Haas, M., Lamour, S., Christ, S. B. & Trapp, O. Mineral-mediated carbohydrate synthesis by mechanical forces in a primordial geochemical setting. *Commun. Chem.* **3**, 140 (2020).
20. Furukawa, Y. et al. Extraterrestrial ribose and other sugars in primitive meteorites. *Proc. Natl Acad. Sci. USA* **116**, 24440–24445 (2019).
21. Furukawa, Y. et al. Bio-essential sugars in samples from asteroid Bennu. *Nat. Geosci.* **19**, 19–24 (2026).
22. Hollis, J. M., Lovas, F. J. & Jewell, P. R. Interstellar glycolaldehyde: the first sugar. *Astrophys. J. Lett.* **540**, L107–L110 (2000).
23. Beltrán, M. T., Codella, C., Viti, S., Neri, R. & Cesaroni, R. First detection of glycolaldehyde outside the Galactic Center. *Astrophys. J. Lett.* **690**, L93–L96 (2009).
24. Jørgensen, J. K. et al. Detection of the simplest sugar, glycolaldehyde, in a solar-type protostar with alma. *Astrophys. J. Lett.* **757**, L4 (2012).
25. Porterfield, J. P. et al. Pyrolysis of the simplest carbohydrate, glycolaldehyde (CHO-CH_2OH), and glyoxal in a heated microreactor. *J. Phys. Chem. A* **120**, 2161–2172 (2016).
26. Cocinero, E. J. et al. Ribose found in the gas phase. *Angew. Chem. Int. Ed.* **51**, 3119–3124 (2012).
27. Peña, I. et al. Six pyranoside forms of free 2-deoxy-D-ribose. *Angew. Chem. Int. Ed.* **52**, 11840–11845 (2013).
28. Insausti, A. et al. Laboratory observation of, astrochemical search for, and structure of elusive erythrulose in the interstellar medium. *J. Phys. Chem. Lett.* **12**, 1352–1359 (2021).
29. Hollis, J. M., Jewell, P. R., Lovas, F. J. & Remijan, A. Green Bank telescope observations of interstellar glycolaldehyde: low-temperature sugar. *Astrophys. J. Lett.* **613**, L45–L48 (2004).

30. Widicus Weaver, S. L. & Blake, G. A. 1,3-Dihydroxyacetone in Sagittarius B2(N-LMH): the first interstellar ketose. *Astrophys. J. Lett.* **624**, L33–L36 (2005).
31. Apponi, A. J. et al. Investigating the limits of chemical complexity in Sagittarius B2(N): a rigorous attempt to confirm 1,3-dihydroxyacetone. *Astrophys. J. Lett.* **643**, L29–L32 (2006).
32. GRAVITY Collaboration. A geometric distance measurement to the Galactic Center black hole with 0.3% uncertainty. *Astron. Astrophys.* **625**, L10 (2019).
33. Requena-Torres, M. A. et al. Organic molecules in the Galactic Center. Hot core chemistry without hot cores. *Astron. Astrophys.* **455**, 971–985 (2006).
34. Zeng, S. et al. Complex organic molecules in the Galactic Centre: the N-bearing family. *Mon. Not. R. Astron. Soc.* **478**, 2962–2975 (2018).
35. Jiménez-Serra, I. et al. Precursors of fatty alcohols in the ISM: discovery of *n*-propanol. *Astron. Astrophys.* **663**, A181 (2022).
36. Sanz-Novo, M. et al. Discovery of the elusive carbonic acid (HOCOOH) in space. *Astrophys. J.* **954**, 3 (2023).
37. Zeng, S. et al. Cloud–cloud collision as drivers of the chemical complexity in Galactic Centre molecular clouds. *Mon. Not. R. Astron. Soc.* **497**, 4896–4909 (2020).
38. Araki, M. et al. A detection of sulfur-bearing cyclic hydrocarbons in space. *Nat. Astron.* **10**, 401A (2026).
39. Martín, S., Requena-Torres, M. A., Martín-Pintado, J. & Mauersberger, R. Tracing shocks and photodissociation in the Galactic Center region. *Astrophys. J.* **678**, 245–254 (2008).
40. Rodríguez-Almeida, L. F. et al. Thiols in the interstellar medium: first detection of HC(O)SH and confirmation of C_2H_5SH. *Astrophys. J. Lett.* **912**, L11 (2021).
41. Rodríguez-Almeida, L. F. et al. First detection of C_2H_5NCO in the ISM and search of other isocyanates towards the G+0.693–0.027 molecular cloud. *Astron. Astrophys.* **654**, L1 (2021).
42. Sanz-Novo, M. et al. Toward the limits of complexity of interstellar chemistry: rotational spectroscopy and astronomical search for n- and i-butanal. *Astron. Astrophys.* **666**, A114 (2022).
43. Snyder, L. E. et al. A rigorous attempt to verify interstellar glycine. *Astrophys. J.* **619**, 914–930 (2005).
44. Halfen, D. T., Apponi, A. J., Woolf, N., Polt, R. & Ziurys, L. M. A systematic study of glycolaldehyde in Sagittarius B2(N) at 2 and 3 mm: criteria for detecting large interstellar molecules. *Astrophys. J.* **639**, 237–245 (2006).
45. Colzi, L. et al. Deuterium fractionation as a multiphase component tracer in the Galactic Center. *Astrophys. J. Lett.* **926**, L22 (2022).
46. Zhang, C. et al. Ionizing radiation exposure on Arrokoth shapes a sugar world. *Proc. Natl Acad. Sci. USA* **121**, e2320215121 (2024).
47. Joshi, P. R. & Lee, Y.-P. Identification of HOC•HC(O)H, $HOCH_2C•O$, and $HOCH_2CH_2O•$ intermediates in the reaction of H + glycolaldehyde in solid para-hydrogen and its implication to the interstellar formation of complex sugars. *J. Am. Chem. Soc.* **146**, 23306–23320 (2024).
48. Wang, J., Marks, J. H., Fortenberry, R. C. & Kaiser, R. I. Interstellar formation of glyceric acid [$HOCH_2CH(OH)COOH$]—the simplest sugar acid. *Sci. Adv.* **10**, eadl3236 (2024).
49. Rodríguez-Fernández, N. J., Martín-Pintado, J., Fuente, A. & Wilson, T. L. ISO observations of the Galactic Center interstellar medium. Neutral gas and dust. *Astron. Astrophys.* **427**, 217–229 (2004).
50. Etxaluze, M. et al. Herschel observations of the Sagittarius B2 cores: hydrides, warm CO, and cold dust. *Astron. Astrophys.* **556**, A137 (2013).
51. Cuppen, H. & Herbst, E. Simulation of the formation and morphology of ice mantles on interstellar grains. *Astrophys. J.* **668**, 294–309 (2007).
52. Cuppen, H., van Dishoeck, E. F., Herbst, E. & Tielens, A. Microscopic simulation of methanol and formaldehyde ice formation in cold dense cores. *Astron. Astrophys.* **508**, 275–287 (2009).
53. Lamberts, T., de Vries, X. & Cuppen, H. The formation of ice mantles on interstellar grains revisited—the effect of exothermicity. *Faraday Discuss.* **168**, 327–347 (2014).
54. Simons, M. A. J., Lamberts, T. & Cuppen, H. M. Formation of COMs through CO hydrogenation on interstellar grains. *Astron. Astrophys.* **634**, A52 (2020).
55. Goto, M. et al. Infrared H3+ and CO studies of the galactic core: GCIRS 3 and GCIRS 1W. *Astrophys. J.* **786**, 96 (2014).
56. Le Petit, F. et al. Physical conditions in the central molecular zone inferred by H_3^+. *Astron. Astrophys.* **585**, A105 (2016).
57. Martín-Pintado, J., de Vicente, P., Fuente, A. & Planesas, P. SiO emission from the Galactic Center molecular clouds. *Astrophys. J. Lett.* **482**, L45–L48 (1997).
58. Jiménez-Serra, I., Caselli, P., Martín-Pintado, J. & Hartquist, T. W. Parametrization of C-shocks. Evolution of the sputtering of grains. *Astron. Astrophys.* **482**, 549–559 (2008).
59. Rivilla, V. M. et al. Ionize hard: interstellar PO+ detection. *Front. Astron. Space Sci.* **9**, 829288 (2022).
60. Sanz-Novo, M. et al. Interstellar detection of O-protonated carbonyl sulfide, $HOCS^+$. *Astrophys. J.* **965**, 149 (2024).
61. Ginsburg, A. et al. JWST reveals widespread CO ice and gas absorption in the Galactic Center cloud G0.253+0.016. *Astrophys. J.* **959**, 36 (2023).
62. Lema-Saavedra, A., Fernández-Ramos, A. & Martínez-Núñez, E. Computational insights into the chemical reaction networks of $C_3H_6O_3$, $C_3H_7O_3$ and $C_2H_5O_2$: implications for the interstellar medium. *Phys. Chem. Chem. Phys.* **27**, 22424–22433 (2025).
63. Fernández-Ruz, M., Jiménez-Serra, I. & Aguirre, J. A theoretical approach to the complex chemical evolution of phosphorus in the interstellar medium. *Astrophys. J.* **956**, 47 (2023).
64. Fried, Z. T. P. et al. Rotational spectrum and first interstellar detection of 2-methoxyethanol using ALMA observations of NGC 6334I. *Astrophys. J. Lett.* **965**, L23 (2024).
65. McGuire, B. A. et al. Discovery of the interstellar chiral molecule propylene oxide (CH_3CHCH_2O). *Science* **352**, 1449–1452 (2016).
66. Islam, S., Bučar, D.-K. & Powner, M. W. Prebiotic selection and assembly of proteinogenic amino acids and natural nucleotides from complex mixtures. *Nat. Chem.* **9**, 584–589 (2017).
67. Nagorski, R. W. & Richard, J. P. Mechanistic imperatives for aldose–ketose isomerization in water: specific, general base- and metal ion-catalyzed isomerization of glyceraldehyde with proton and hydride transfer. *J. Am. Chem. Soc.* **123**, 794–802 (2001).
68. Colville, B. W. F. & Powner, M. W. Selective prebiotic synthesis of α-threofuranosyl cytidine by photochemical anomerization. *Angew. Chem. Int. Ed.* **60**, 10526–10530 (2021).
69. Altwegg, K., Balsiger, H. & Fuselier, S. A. Cometary chemistry and the origin of icy Solar System bodies: the view after Rosetta. *Annual Rev. Astron. Astrophys.* **57**, 113–155 (2019).
70. Ligterink, N. F. W. et al. The rapid formation of macromolecules in irradiated ice of protoplanetary disk dust traps. *Nat. Astron.* **8**, 1257–1263 (2024).
71. Cronin, J. R. & Pizzarello, S. Enantiomeric excesses in meteoritic amino acids. *Science* **275**, 951–955 (1997).
72. Cooper, G. & Rios, A. C. Enantiomer excesses of rare and common sugar derivatives in carbonaceous meteorites. *Proc. Natl Acad. Sci. USA* **113**, E3322–E3331 (2016).
73. Ribó, J. M. & Hochberg, D. Chemical basis of biological homochirality during the abiotic evolution stages on Earth. *Symmetry* **11**, 814 (2019).
74. Whittet, D. C. B. & Duley, W. W. Carbon monoxide frosts in the interstellar medium. *Astron. Astrophys. Rev.* **2**, 167–189 (1991).

75. Piani, L. et al. Earth's water may have been inherited from material similar to enstatite chondrite meteorites. *Science* **369**, 1110–1113 (2020).
76. Chyba, C. & Sagan, C. Endogenous production, exogenous delivery and impact-shock synthesis of organic molecules: an inventory for the origins of life. *Nature* **355**, 125–132 (1992).
77. Koeberl, C. Impact processes on the early Earth. *Elements* **2**, 211–216 (2006).
78. Cartwright, J., Hodges, K. & Wadhwa, M. Evidence against a late heavy bombardment event on vesta. *Earth Planet. Sci. Lett.* **590**, 117576 (2022).
79. Wogan, N. F., Catling, D. C. & Zahnle, K. J. Timing and likelihood of the origin of life derived from post-impact highly reducing atmospheres. *Astrobiology* **24**, 881–891 (2024).
80. McCaffrey, V. P., Zellner, N. E. B., Waun, C. M., Bennett, E. R. & Earl, E. K. Reactivity and survivability of glycolaldehyde in simulated meteorite impact experiments. *Origins Life Evol. Biosphere* **44**, 29–42 (2014).
81. Zellner, N. E., McCaffrey, V. P. & Butler, J. H. Cometary glycolaldehyde as a source of pre-rna molecules. *Astrobiology* **20**, 1377–1388 (2020).
82. Yu, H., Zhang, S. & Chaput, J. Darwinian evolution of an alternative genetic system provides support for TNA as an RNA progenitor. *Nat. Chem.* **4**, 183–187 (2012).
83. Tercero, F. et al. Yebes 40 m radio telescope and the broad band Nanocosmos receivers at 7 mm and 3 mm for line surveys. *Astron. Astrophys.* **645**, A37 (2021).
84. Megías, A. et al. The complex organic molecular content in the L1517B starless core. *Mon. Not. R. Astron. Soc.* **519**, 1601–1617 (2023).
85. Martín, S. et al. Spectral Line Identification and Modelling (SLIM) in the MAdrid Data CUBe Analysis (MADCUBA) package. Interactive software for data cube analysis. *Astron. Astrophys.* **631**, A159 (2019).
86. Lattanzi, V. et al. Advancing spectroscopic understanding of $HOCS^+$: laboratory investigations and astronomical implications. *Astron. Astrophys.* **689**, A260 (2024).
87. Rey-Montejo, M. et al. Discovery of MgS and NaS in the interstellar medium and tentative detection of CaO. *Astrophys. J.* **975**, 174 (2024).
88. Massalkhi, S. et al. The first detection of SiC_2 in the interstellar medium. *Astron. Astrophys.* **678**, A45 (2023).
89. Li, J. et al. Widespread presence of glycolaldehyde and ethylene glycol around Sagittarius B2. *Astrophys. J.* **849**, 115 (2017).
90. Frisch, M. J. et al. Gaussian 16 Revision A.03 (Gaussian, 2016).
91. Zhao, Y. & Truhlar, D. G. Design of density functionals that are broadly accurate for thermochemistry, thermochemical kinetics, and nonbonded interactions. *J. Phys. Chem. A* **109**, 5656–5667 (2005).
92. Stewart, J. J. P. Optimization of parameters for semiempirical methods VI: more modifications to the NDDO approximations and re-optimization of parameters. *J. Mol. Model.* **19**, 1–32 (2013).
93. Rappe, A. K., Casewit, C. J., Colwell, K. S., Goddard, W. A. I. & Skiff, W. M. UFF, a full periodic table force field for molecular mechanics and molecular dynamics simulations. *J. Am. Chem. Soc.* **114**, 10024–10035 (1992).
94. Weigend, F. & Ahlrichs, R. Balanced basis sets of split valence, triple zeta valence and quadruple zeta valence quality for H to Rn: design and assessment of accuracy. *Phys. Chem. Chem. Phys.* **7**, 3297–3305 (2005).
95. Roos, B. O., Taylor, P. R. & Sigbahn, P. E. A complete active space SCF method (CASSCF) using a density matrix formulated super-CI approach. *Chem. Phys.* **48**, 157–173 (1980).
96. Neese, F., Wennmohs, F., Becker, U. & Riplinger, C. The ORCA quantum chemistry program package. *JChPh* **152**, 224108 (2020).
97. Ferro-Costas, D., Truhlar, D. G. & Fernández-Ramos, A. Pilgrim-version 2020.2 (University of Minneapolis, Universidade de Santiago de Compostela, 2020).
98. Eckart, C. The penetration of a potential barrier by electrons. *PhRv* **35**, 1303 (1930).
99. Marcus, R. A. Chemical and electrochemical electron-transfer theory. *Annu. Rev. Phys. Chem.* **15**, 155–196 (1964).
100. Marcus, R. & Sutin, N. Electron transfers in chemistry and biology. *Biochim. Biophys. Acta Rev. Bioenerg.* **811**, 265–322 (1985).
101. Ioppolo, S. et al. A non-energetic mechanism for glycine formation in the interstellar medium. *Nat. Astron.* **5**, 197–205 (2021).
102. Álvarez-Barcia, S., Russ, P., Kästner, J. & Lamberts, T. Hydrogen transfer reactions of interstellar complex organic molecules. *Mon. Not. R. Astron. Soc.* **479**, 2007 (2018).
103. Holdship, J., Viti, S., Jiménez-Serra, I., Makrymallis, A. & Priestley, F. UCLCHEM: a gas-grain chemical code for clouds, cores, and C-shocks. *Astron. J.* **154**, 38 (2017).
104. Jiménez-Serra, I. et al. Detection of a four-carbon sugar in interstellar space. *Zenodo* https://doi.org/10.5281/zenodo.20081358 (2026).

Acknowledgements

We thank the Yebes 40 m and IRAM 30 m staff for their support during the observations. This work is based on observations carried out with the Yebes 40 m telescope (project 21A014) and the IRAM 30 m telescope (projects 123-22, 076-23). The 40 m radio telescope at Yebes Observatory is operated by the Spanish Geographic Institute (IGN; Ministerio de Transportes y Movilidad Sostenible). IRAM is supported by INSU/CNRS (France), MPG (Germany) and IGN (Spain). Computational resources were provided by CENITS and Foundation Computaex through the High-Performance Computing facility LUSITANIA-II, which are greatly appreciated.

Author contributions

I.J.-S. initiated and managed the project. She wrote the observational part of the manuscript, together with the abstract, introduction and concluding parts. J.G.d.l.C. wrote the part of the quantum chemical calculations, while H.M.C. carried out the KMC simulations and wrote that part of the manuscript. M.R.-M. contributed creating the figures and tables and provided comments to an initial draft. M.S-N., V.M.R., J.M.-P., L.C., S.Z., S.M., M.A.R.-T., B.T., P.d.V., A.M.-H., A.M., A. L.-G. and D.S.A. contributed to the acquisition and reduction of the astronomical data as well as providing comments to the manuscript. C.B. investigated the biochemical relevance of erythrulose and other sugars in the context of the origin of life and contributed to the manuscript. E.J.C., A.I. and E.R.A. provided the SPCAT-format spectroscopic predictions of erythrulose, enabling its identification in the astronomical data. J.S. performed the UCLCHEM gas-phase simulations and contributed to the KMC simulations. E.J.C. contributed to the scientific discussion and thoroughly revised a previous version of the manuscript, and together with A.I. and E.R.A. also commented on the paper.

Funding

This work is supported by ERC grant OPENS, GA no. 101125858 funded by the European Union. Views and opinions expressed are, however, those of the author(s) only and do not necessarily reflect those of the European Union or the European Research Council Executive Agency. Neither the European Union nor the granting authority can be held responsible for them. I.J-.S., J.G.d.l.C., M.S.-N., V.M.R., J.M.-P., L.C., S.Z., S.M., A.M., A.M.-H., A.L.-G., M.A.R.-T. and D.S.A. also acknowledge partial support from grant number PID2022-136814NB-I00 funded by the Spanish

Ministry of Science, Innovation and Universities/State Agency of Research MICIU/AEI/ 10.13039/501100011033 and by 'ERDF/EU'. I.J-.S., A.M. and S.Z. acknowledge partial support from the CSIC Bilateral project SOULMATE (BIJSP25017). J.G.d.l.C. acknowledges support from European Funds for Regional Development and the Autonomous Government of Extremadura (grant no. GR24020). M.S.-N. also acknowledges a Juan de la Cierva Postdoctoral Fellowship, project JDC2022-048934-I, funded by MCIN/AEI/10.13039/501100011033 and by the European Union 'NextGenerationEU/PRTR', and a Humboldt Research Fellowship funded by the Alexander von Humboldt foundation. V.M.R. aknowledges support through grant RYC2020-029387-I funded by MICIU/AEI/10.13039/501100011033 and by 'ESF, Investing in your future', and from the Consejo Superior de Investigaciones Científicas (CSIC) and the Centro de Astrobiología (CAB) through the project 20225AT015 (Proyectos intramurales especiales del CSIC). V.M.R. and D.S.A. acknowledge support from grant CNS2023-144464 funded by MICIU/AEI/10.13039/501100011033 and by 'European Union NextGenerationEU/PRTR'. D.S.A. acknowledges the financial support provided by the Comunidad de Madrid through the grant PIPF-2022/TEC-25475. L.C. acknowledges support from a research fellowship from the 'la Caixa' Foundation (ID 100010434 – fellowship code LCF/BQ/PR25/12110012). B.T. acknowledges Spanish Ministry of Science support from grants PID2022-137980NB-100 and PID2023-147545NB-I00. A.L-G. and D.S.A acknowledge support from the Consejo Superior de Investigaciones Científicas (CSIC) and the Centro de Astrobiología (CAB) through the project 20225AT015 (Proyectos intramurales especiales del CSIC). E.J.C. acknowledges support from the Basque Government (project IT1491-22) and from grant PID2023-147698NB-I00 funded by MCIN/AEI/10.13039/501100011033 and ERDF/EU, and the CSIC I-LINK project ILINK25125.

Competing interests
The authors declare no competing interests.

Additional information
Extended data is available for this paper at https://doi.org/10.1038/s41550-026-02905-7.

Supplementary information The online version contains supplementary material available at https://doi.org/10.1038/s41550-026-02905-7.

Correspondence and requests for materials should be addressed to Izaskun Jiménez-Serra.

Peer review information *Nature Astronomy* thanks the anonymous reviewer(s) for their contribution to the peer review of this work. Peer reviewer reports are available.

Reprints and permissions information is available at www.nature.com/reprints.

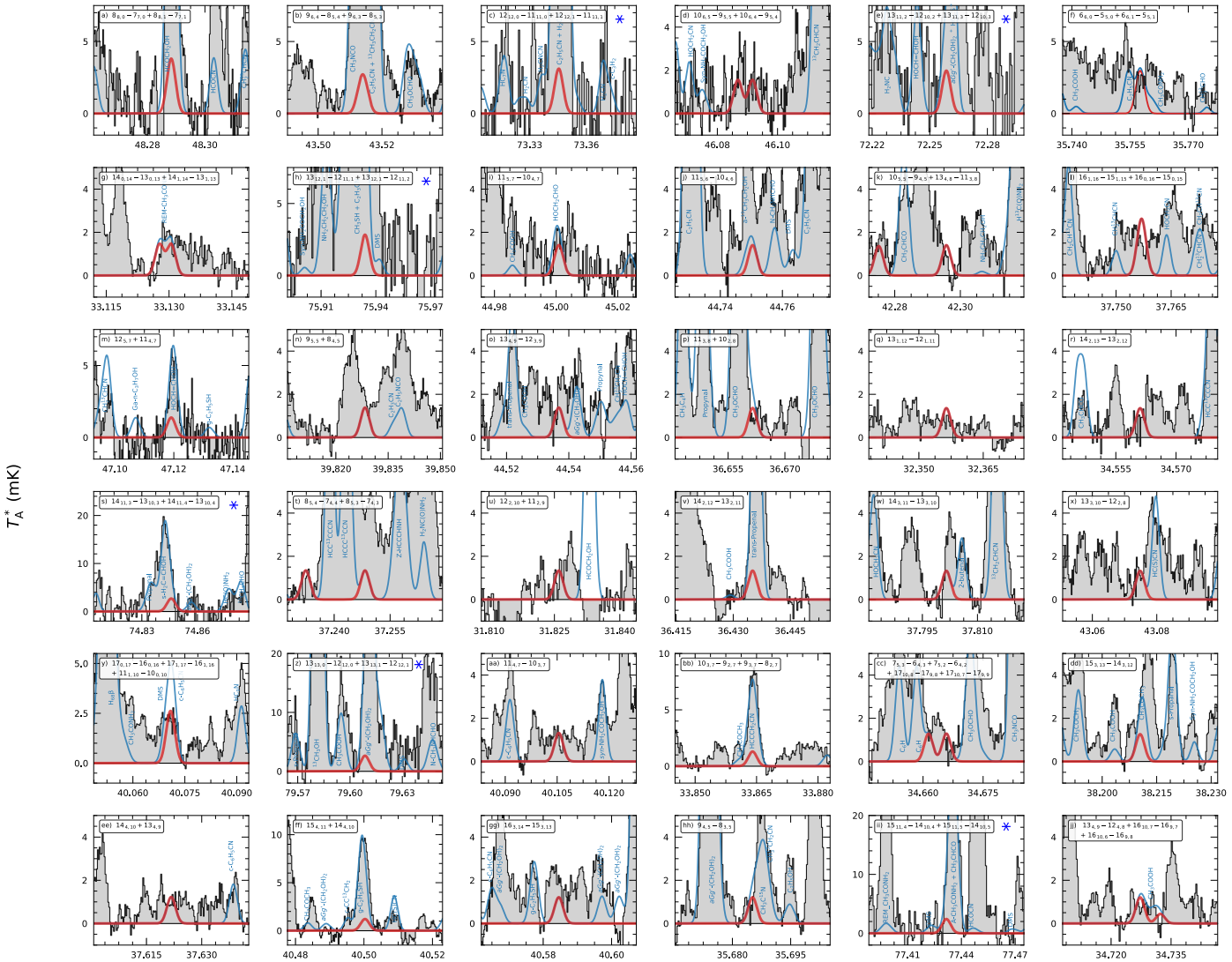
Publisher's note Springer Nature remains neutral with regard to jurisdictional claims in published maps and institutional affiliations.

Open Access This article is licensed under a Creative Commons Attribution 4.0 International License, which permits use, sharing, adaptation, distribution and reproduction in any medium or format, as long as you give appropriate credit to the original author(s) and the source, provide a link to the Creative Commons licence, and indicate if changes were made. The images or other third party material in this article are included in the article's Creative Commons licence, unless indicated otherwise in a credit line to the material. If material is not included in the article's Creative Commons licence and your intended use is not permitted by statutory regulation or exceeds the permitted use, you will need to obtain permission directly from the copyright holder. To view a copy of this licence, visit http://creativecommons.org/licenses/by/4.0/.

© The Author(s) 2026, modified publication 2026

[1]Center for Astrobiology (CAB), CSIC-INTA, Torrejón de Ardoz, Spain. [2]Departamento de Química Orgánica e Inorgánica, Facultad de Ciencias and IACYS-Green Chemistry and Sustainable Development Unit, University of Extremadura, Badajoz, Spain. [3]Institute for Molecules and Materials, Radboud University, Nijmegen, the Netherlands. [4]Departamento de Física de la Tierra y Astrofísica, Facultad de Ciencias Físicas, Universidad Complutense de Madrid, Madrid, Spain. [5]Center for Astrochemical Studies, Max-Planck-Institut für extraterrestrische Physik, Garching bei Munchen, Germany. [6]Star and Planet Formation Laboratory, Cluster for Pioneering Research, Wako, Japan. [7]European Southern Observatory, Santiago, Chile. [8]Joint ALMA Observatory, Santiago, Chile. [9]Department of Physics, Astronomy and Geosciences, Towson University, Towson, MD, USA. [10]Observatorio Astronómico Nacional (OAN-IGN), Madrid, Spain. [11]Observatorio de Yebes (OY-IGN), Yebes, Spain. [12]Department of Physical Chemistry, Faculty of Science and Technology, University of the Basque Country (EHU), Leioa, Spain. [13]Biofisika Institute, CSIC, EHU, Leioa, Spain. [14]Grupo de Espectroscopía Molecular, Edificio Quifima, Laboratorios de Espectroscopía y Bioespectroscopía, Universidad de Valladolid, Valladolid, Spain. ✉e-mail: ijimenez@cab.inta-csic.es

https://doi.org/10.1038/s41550-026-02905-7



Extended Data Fig. 1 | Remaining erythrulose transitions present in our dataset with peak intensities ≥1.2 mK. Filled histograms report the observed spectra, red lines show the line profiles of the erythrulose transitions fitted with MADCUBA-SLIM, and blue lines present the total fit to the spectra considering all the molecules identified toward G+0.693. The quantum numbers of each transition of erythrulose are given in the upper part of each panel. In blue, we label the molecular species contributing to the observed spectra in the vicinity of the erythrulose lines. Blue asterisks indicate those transitions covered within the 3mm atmospheric window.

https://doi.org/10.1038/s41550-026-02905-7

Extended Data Table 1 | Spectroscopic information of the erythrulose transitions shown in Fig. 1

Frequency (MHz)	Transition $(J', K'_{-1}, K'_{+1} \rightarrow J'', K''_{-1}, K''_{+1})$	Log I (nm^2MHz)	E_{low} (cm^{-1})	rms (mK)	$\int T_A^* dv$ (mK km s^{-1})	S/N	Residual	Blending
42023.08 (0.12)	7,7,0→6,6,0	-6.339	4.0	0.4	81.9	32	25%	**mostly unblended**
42023.08 (0.12)	7,7,1→6,6,1	-6.339	4.0	0.4				
44611.73 (0.12)	8,7,1→7,6,1	-6.279	4.6	0.6	81.6	22	37%	blended (c-C_6H_5CN)
44611.73 (0.12)	8,7,2→7,6,2	-6.279	4.6	0.6				
40931.91 (0.07)	8,6,2→7,5,2	-6.407	4.0	0.5	72.7	23	13%	**mostly unblended**
40932.25 (0.07)	8,6,3→7,5,3	-6.407	4.0	0.5				
38345.96 (0.07)	7,6,1→6,5,1	-6.478	3.3	0.3	71.4	36	40%	blended $HCCCH_2CN$
38346.02 (0.07)	7,6,2→6,5,2	-6.478	3.3	0.3				
35442.28 (0.06)	15,1,15→14,1,14	-6.274	8.4	0.4	66.8	24	20%	**mostly unblended**
35443.77 (0.06)	15,0,15→14,0,14	-6.274	8.4	0.4				
39782.32 (0.04)	9,5,4→8,4,4	-6.462	4.1	0.3	32.4	17	8%	**mostly unblended**
34639.84 (0.04)	14,1,13→13,1,12	-6.333	7.9	0.5	31.9	9	35%	blended (U-line)
32227.63 (0.03)[a]	13,2,12→12,2,11	-6.427	6.8	0.5	31.7	9	20%	blended $(CH_2OH)_2$
40329.80 (0.07)	15,3,12→14,3,11	-6.180	9.9	0.5	30.2	9	24%	**mostly unblended**
33385.03 (0.03)	13,3,11→12,3,10	-6.408	7.3	0.5	30.1	9	18%	**mostly unblended**
39073.86 (0.05)	15,4,12→14,4,11	-6.222	10.1	0.4	27.6	10	49%	blended (U-line)
37059.88 (0.02)	10,3,8→9,2,8	-6.635	4.1	0.4	23.6	9	52%	blended (U-line)

The S/N ratio is computed from the integrated signal $\int(T_A^* \, dv)$ and its associated noise level, $\sigma = \text{rms} \times \sqrt{(\delta v \times \text{FWHM})}$, where δv is the velocity resolution of the spectra and the FWHM is fitted from the data. We also provide the contribution of the contamination to the overall area after subtracting the LTE fit of erythrulose from the observed spectrum over a velocity range of ± FWHM (Residual area in %). We consider that the observed feature is mostly unblended if the residual area is ≤25%. A similar approach has been adopted in recent detections of complex organic molecules in line rich sources[38]. Note (a) indicates that the line is considered blended although the residual area is ≤25%, because of a close $(CH_2OH)_2$ line. Values in parenthesis in the first column correspond to frequency uncertainties given in units of MHz.